



X-ray magnetic circular dichroism in RuO₂

A. Hariki ¹, Y. Takahashi,¹ and J. Kuneš ^{2,3}

¹*Department of Physics and Electronics, Graduate School of Engineering, Osaka Metropolitan University, 1-1 Gakuen-cho, Nakaku, Sakai, Osaka 599-8531, Japan*

²*Institute for Solid State Physics, TU Wien, 1040 Vienna, Austria*

³*Department of Condensed Matter Physics, Faculty of Science, Masaryk University, Kotlářská 2, 611 37 Brno, Czechia*



(Received 5 December 2023; accepted 23 February 2024; published 11 March 2024)

We present a numerical simulation of the x-ray magnetic circular dichroism (XMCD) of the $L_{2,3}$ and $M_{2,3}$ edges of Ru in antiferromagnetic RuO₂ using a combination of density functional plus dynamical mean-field theory and configuration interaction treatment of the Anderson impurity model. We study the dependence of the dichroic spectra on the orientation of the Néel vector and discuss it in the context of altermagnetism. An approximate equivalence between the XMCD spectra for geometries with x rays propagating parallel and perpendicular to the Néel vector is found and shown to be exact in the absence of valence spin-orbit coupling and a core-valence multipolar interaction.

DOI: [10.1103/PhysRevB.109.094413](https://doi.org/10.1103/PhysRevB.109.094413)

I. INTRODUCTION

Recently, a metallic compensated magnet RuO₂ has attracted considerable attention. The combination of its rutile structure with an antiparallel ordering of spin moments gives rise to a number of phenomena such as the anomalous Hall effect (AHE) [1–8] or charge-spin conversion effects [9–16], and strongly spin-polarized electronic band structures [2,6,9,15,17–23], unusual among compensated collinear magnets. Moreover, some of these effects depend on the orientation of the Néel vector \mathbf{L} and may be switched by manipulating it. The term altermagnet [9,15] was introduced for RuO₂ and similar materials to reflect the alternating spin polarization in the momentum space.

Altermagnetism is a nonrelativistic concept, i.e., it relies on the spin rotation SU(2) symmetry of the Hamiltonian in the absence of spin-orbit coupling (SOC). However, the above transport and charge-excitation effects are possible only if altermagnetic order and SOC are present simultaneously. The SOC thus plays a dual role. On one hand, it allows the altermagnetic order to be detectable through some of the technologically interesting transport effects. On the other hand, it gives rise to magnetocrystalline anisotropy and possibly a weak ferromagnetism with a small net magnetization \mathbf{m} . To prove the altermagnetic origin of transport phenomena, e.g., AHE, one must not only measure a finite signal, but also distinguish the altermagnetic contribution associated with \mathbf{L} from the contribution due to weak ferromagnetism or possibly the external magnetic field associated with \mathbf{m} , which requires a careful quantitative analysis [24].

The x-ray magnetic circular dichroism (XMCD) provides an alternative. The XMCD is an odd magneto-optical effect, which arises from the same antisymmetric part of the conductivity tensor $\sigma^a = \frac{1}{2}(\sigma - \sigma^T)$ as the valence band phenomena, such as AHE or magneto-optical effects in the visible range and therefore follows the same symmetry rules. However,

the XMCD, especially in lighter elements, arises due to the SOC in the core state and is only weakly affected by the valence SOC reflecting the typically small orbital moments [25–27]. The theoretical altermagnetic contribution to XMCD can be obtained as the XMCD with the valence SOC switched off. In other words, in the x-ray spectral range it is the core SOC which allows the altermagnetic order to be expressed in the magneto-optical spectra, while the valence SOC, which causes the spurious weak ferromagnetism, has only a marginal contribution [28]. In the optical or transport effects the valence SOC plays a dual role, which cannot be resolved by simply switching it off.

In this paper we compute XMCD at $L_{2,3}$ and $M_{2,3}$ edges of Ru for various orientations of the Néel vector \mathbf{L} , see Fig. 1. Recently, Sasabe *et al.* [29] calculated XMCD in RuO₂ using the atomic model in an external Zeeman field, and discussed their results in the context of a strong-coupling (insulator) picture of an excitonic magnet [30]. Our calculation of XMCD is performed for the antiferromagnetic metallic state [17] obtained with the density functional plus dynamical mean-field theory (DFT+DMFT) [31–33]. The method identifies a Fermi-surface instability as the origin of the antiferromagnetism of metallic RuO₂ [17].

II. COMPUTATIONAL METHOD

Starting with a density functional theory (DFT) calculation for the experimental structure of RuO₂ [34] using WIEN2K [35], we construct a multiband Hubbard model [36,37] spanning the Ru $4d$ states. The Ru $4d$ crystal field levels are summarized in Table I. The electron-electron interaction within the Ru d shell is parametrized by $U = 3.0$ eV and $J = 0.45$ eV. The interaction parameters affect the magnitude of the ordered Ru moment [17], and thus the XMCD intensities, as examined in the Supplemental Material (SM) [38] (see also Refs. [39–44] therein). We use the same DMFT implementation for the multiband Hubbard model as in

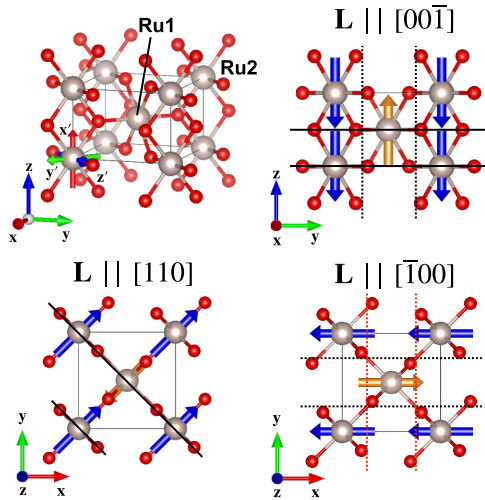


FIG. 1. Crystal structure of RuO_2 and orientations of magnetic structures studied in this work. Solid (dashed) lines indicate the mirror (glide) plane m .

Refs. [45–47]. Material-specific details can be found in SM [38].

The XMCD spectra are calculated for (i) the Ru^{4+} atomic model and (ii) DMFT plus Anderson impurity model (AIM) using the method of Refs. [45–47] based on a configuration interaction impurity solver. The two models implement the same atomic Hamiltonian, which is coupled to an electronic bath via the hybridization function $\Delta(\omega)$ in (ii). The ordered Ru moments are generated by the (self-consistently determined) spin-polarized bath in (ii). In (i) we impose a Zeeman field chosen to generate the same moment as obtained in (ii). A detailed comparison of the two models in SM [38] reveals similar spectra. The computationally cheap atomic model is therefore used for the symmetry analysis of the results.

The SOC is not included in the DMFT self-consistent calculations. However, SOC within the Ru $4d$ shell is included in the AIM when computing the XMCD intensities. The spin-polarized hybridization densities $\Delta(\omega)$ are transformed to capture the desired Néel vector orientations in these simulations.

III. RESULTS

The XMCD is the difference of the absorption spectra for the right-hand and left-hand circularly polarized light propagating along the direction $\hat{\mathbf{k}}$. It is convenient to view the antisymmetric part of the conductivity tensor σ as an axial (Hall) vector $\mathbf{h}(\omega) = [\sigma_{zy}^a(\omega), \sigma_{xz}^a(\omega), \sigma_{yx}^a(\omega)]$. For simplicity we will not show the ω dependence from now on, but indicate

TABLE I. The Ru $4d$ orbital energies in RuO_2 derived from the DFT calculation for the experimental rutile structure. The $4d$ orbitals are represented in a local coordinate ($x'y'z'$) in the left top panel of Fig. 1.

	d_{xy}	$d_{3z^2-r^2}$	$d_{x^2-y^2}$	d_{zx}	d_{yz}
Energy (eV)	3.283	3.522	-0.127	0.036	0.067

the dependence on $\hat{\mathbf{k}}$ as well as the orientation of the Néel vector \mathbf{L} ,

$$\Delta F(\hat{\mathbf{k}}, \mathbf{L}) = F^+(\hat{\mathbf{k}}, \mathbf{L}) - F^-(\hat{\mathbf{k}}, \mathbf{L}) = 2 \text{Im} \mathbf{h}(\mathbf{L}) \cdot \hat{\mathbf{k}}. \quad (1)$$

The Hall vector $\mathbf{h}(\mathbf{L})$ contains information about XMCD for any direction \mathbf{k} , but depends on the crystallographic orientation of \mathbf{L} . In Fig. 2 we show the elements of σ at the Ru $M_{2,3}$ edge for \mathbf{L} along the $[00\bar{1}]$, $[110]$, and $[\bar{1}00]$ directions.

Owing to the local nature of core-level excitations the observed signal is given by a sum of contributions from the two Ru sites [48]. Depending on the orientation of \mathbf{L} , the two Ru sites are connected by some relativistic symmetry operation or not. In the former case XMCD may vanish due to cancellation between the site contributions even if these are nonzero. In the latter case a nonzero XMCD exists if allowed locally by the site symmetry.

A. Symmetry considerations

In the following we will make use of mirror symmetries to discuss the dependence of the XMCD signal, i.e., $\mathbf{h}(\mathbf{L})$ as a function of \mathbf{L} . The mirror (glide) planes are marked in Fig. 1. XMCD is forbidden if there is a mirror plane parallel to the x-ray wave vector \mathbf{k} , since it maps the right-hand circular polarization on the left-hand one and vice versa. Since the local moments transform as axial vectors, a crystallographic mirror (glide) plane m is retained as an element of the relativistic symmetry group either if m is parallel to \mathbf{L} and maps the magnetic sublattices on one another or m is perpendicular to \mathbf{L} and maps each magnetic sublattice on itself. Using these simple rules we can understand the behavior of the calculated XMCD.

For $\mathbf{L} \parallel [110]$ the two Ru sites are inequivalent. There is no symmetry relationship between the XMCD contributions from the two Ru sites and therefore no cancellation between the site contributions $\mathbf{h}^{(i=1,2)}$ as shown in Fig. 3. The total XMCD signal is nonzero unless XMCD is symmetry forbidden locally on each site. The mirror plane $m_{(110)}$ maps each Ru site on itself and is perpendicular to the local moments, which implies that only $\mathbf{h}^{(i)} \parallel [110]$ is allowed.

For both $\mathbf{L} \parallel [00\bar{1}]$ and $\mathbf{L} \parallel [\bar{1}00]$ the two Ru sites are equivalent. For $\mathbf{L} \parallel [00\bar{1}]$ the presence of two nonparallel mirror planes, the glide planes $n_{(100)}$ and $n_{(010)}$ mapping the two Ru sites on each other, forbids the total XMCD signal for any direction of \mathbf{k} : $\mathbf{h}^{(1)} = -\mathbf{h}^{(2)}$. Moreover, the mirror plane $m_{(001)}$ implies that $h_x^{(i)} = h_y^{(i)} = 0$ on each site as shown in Fig. 3. For $\mathbf{L} \parallel [\bar{1}00]$, the glide plane $n_{(010)}$ implies $h_z^{(1)} = -h_z^{(2)}$ and $h_x^{(1)} = -h_x^{(2)}$ (see Fig. 3). The glide plane $n_{(100)}$, indicated by the red dashed lines in Fig. 1, which maps the two Ru sites on each other, must be coupled with the time reversal $n_{(100)}\mathcal{T}$ in order to be a symmetry operation. Therefore the two Ru sites yield the same contribution $h_y^{(1)} = h_y^{(2)}$ (see Fig. 3). Finally, we observe that $h_z^{(i)} = 0$ locally owing to the mirror plane times time-reversal operations $m_{(001)}\mathcal{T}$.

B. L and M edge of RuO_2

Figure 4 shows Ru $L_{2,3}$ - and $M_{2,3}$ -edge absorption spectra with left and right circularly polarized x rays and the XMCD intensities calculated using the local density approximation

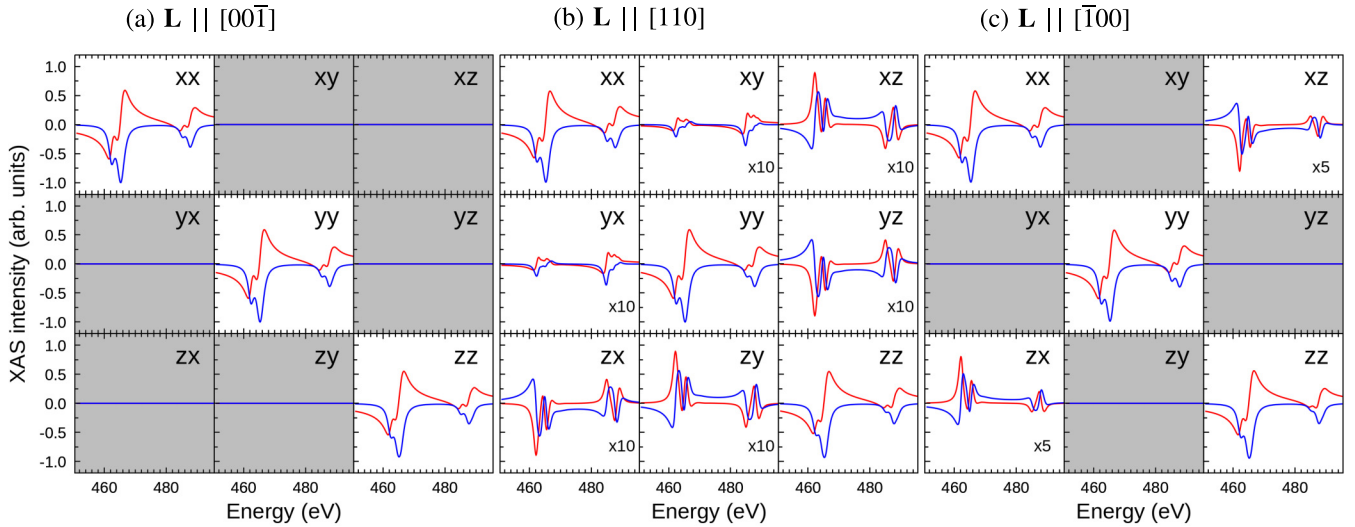


FIG. 2. Real (red) and imaginary (blue) part of the optical conductivity tensor at the Ru $M_{2,3}$ edge for different orientations of the Néel vector \mathbf{L} . Here, the Ru⁴⁺ atomic model ($J = 0.50$ eV) is used.

plus DMFT (LDA+DMFT) AIM method. The L - and M -edge spectra have similar shapes consisting of a main peak and a shoulder, indicated by vertical lines [49], and agree well with the available experimental absorption data on the $M_{2,3}$ edges [50]. The shoulders arise from the Ru t_{2g} bands, which host the spin moment. The e_g bands are spin split but empty. Consequently, the XMCD intensities are largely concentrated in the shoulder for all $M_{2,3}$ and $L_{2,3}$ edges. A similar shape of the XMCD spectra was observed on the $M_{2,3}$ -edge XMCD of SrRuO₃, a prototypical ferromagnetic metallic Ru⁴⁺ oxide [51].

Our results show that a nonzero XMCD exists for $\mathbf{L} \parallel [110]$ and any \mathbf{k} not perpendicular to \mathbf{L} as well as $\mathbf{L} \parallel [\bar{1}00]$ and \mathbf{k} not perpendicular to $[010]$. On the other hand, the XMCD signal vanishes for the experimental easy axis $\mathbf{L} \parallel [00\bar{1}]$. It was shown that \mathbf{L} can be tilted in the $[110]$ using an external magnetic field [24]. While we have included the

valence SOC in the calculation of the XMCD spectra using both methods (i) and (ii), we did not include the magnetocrystalline anisotropy in our calculations. Therefore we can only speculate about the external field effect. Looking at the site contributions for the $\mathbf{L} \parallel [110]$ in Fig. 3 we observe that site 1 dominates over site 2. Assuming that the external field has only a moderate influence on the size of the local moments,

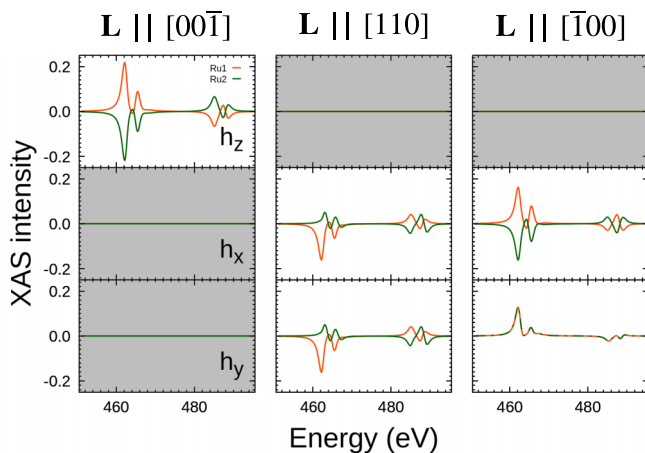


FIG. 3. The imaginary part of the Hall vectors $\mathbf{h}^{(i)}$ at the Ru $M_{2,3}$ edge for site 1 (yellow) and site 2 (green) obtained for different orientations of the Néel vector \mathbf{L} . Here, the Ru⁴⁺ atomic model ($J = 0.50$ eV) is used. The XMCD spectra of the Ru⁴⁺ atomic model are found in SM [38].

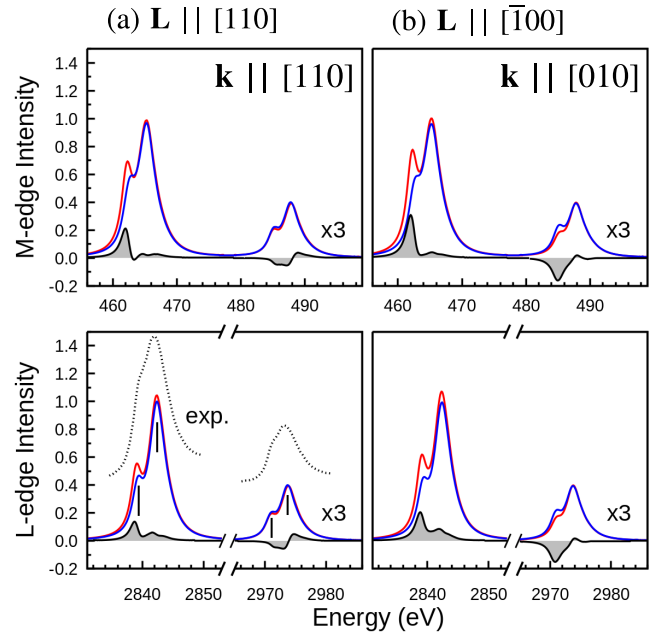


FIG. 4. The x-ray absorption spectroscopy (XAS) calculated for the two circular polarizations (red and blue) at the Ru $M_{2,3}$ edge (top) and $L_{2,3}$ edge (bottom) together with the XMCD intensities (shaded) calculated for different orientations of the Néel vector \mathbf{L} and x-ray propagation vector \mathbf{k} using the LDA+DMFT AIM method. The calculated spectral intensities are broadened by a Lorentzian of 1.0 eV [half width at half maximum (HWHM)]. The experimental L_3 -edge x-ray absorption spectrum is taken from Ref. [49]. The L_3 main line and shoulder feature are indicated by vertical lines.

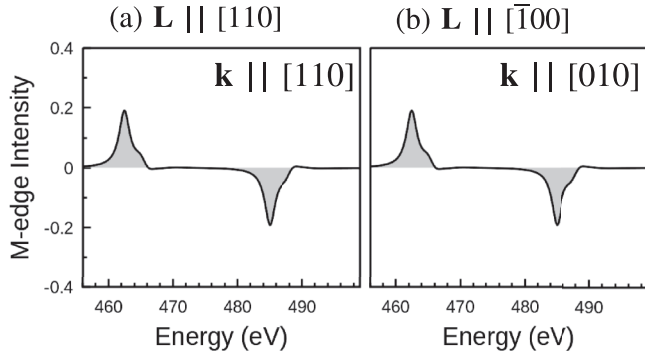


FIG. 5. Ru $M_{2,3}$ -edge XMCD intensities $\Delta F^{(a)}$ in case (a) and $\Delta F^{(b)}$ in case (b) calculated without SOC within the Ru $4d$ shell and $3p - 4d$ core-valence multiplet interaction for the two different Néel vectors \mathbf{L} and x-ray propagation vectors $\hat{\mathbf{k}}$ by the LDA+DMFT AIM method.

we may conclude that it does not alter the present result substantially.

C. No valence SOC, no core-valence multipole interaction

Comparing the XMCD spectra in Figs. 4(a) and 4(b) we observe a similarity pronounced in particular on the L_3 and M_3 edges. In Fig. 5 we show that this is not accidental. In Ref. [28] we have observed that turning off the valence SOC and the multipole part of the core-valence interaction may change the XMCD spectra qualitatively. This is because the Hamiltonian without these interactions possesses a higher symmetry. In the present case, switching off the valence SOC and the multipole part of the core-valence interaction results in an equality of the two spectra $\Delta F^{(a)}(\omega) = \Delta F^{(b)}(\omega)$. This may appear surprising given the apparently different geometry in case (a) $\mathbf{k} \parallel \mathbf{L}$ while in case (b) $\mathbf{k} \perp \mathbf{L}$. In the Appendix we provide an analytic proof, which uses only the presence of twofold axes along the $[110]$ and $[1\bar{1}0]$ directions.

IV. CONCLUSIONS

We have calculated the XMCD spectra on the Ru $L_{2,3}$ and $M_{2,3}$ edges of antiferromagnetic RuO_2 using the LDA+DMFT approach. The present XMCD spectra differ from the recent calculations using the atomic model [29]. The origin of this discrepancy can be traced to different values of the crystal field and Hund's coupling parameters. We have analyzed the symmetry of the XMCD spectra for various orientations of the Néel vector. The results apply to any collinear antiferromagnet with the rutile structure. No XMCD is allowed for the easy axis $[001]$ orientation of the Néel vector \mathbf{L} . We have predicted the XMCD spectra for the experimentally accessible $[110]$ orientation.

ACKNOWLEDGMENTS

We thank A. Smolyanyuk and A. Kauch for discussions and a critical reading of the manuscript. A.H. was supported by JSPS KAKENHI Grants No. 21K13884, No. 21H01003, No. 23K03324, and No. 23H03817, and the 2023 Osaka Metropolitan University (OMU) Strategic Research

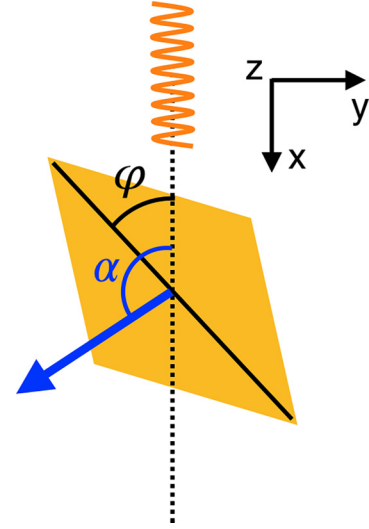


FIG. 6. Geometry used to prove the equality of $\Delta F^{(a)}$ and $\Delta F^{(b)}$ numerically observed in Fig. 4. The Ru atom is located in the center, and the parallelogram (long axis parallel to $[110]$) represents the orientation of the crystal.

Promotion Project for Younger Researcher. J.K. was supported by the project Quantum materials for applications in sustainable technologies (QM4ST), funded as Project No. CZ.02.01.01/00/22_008/0004572 by Programme Johannes Amos Comenius, call Excellent Research.

APPENDIX: XMCD WITH NO CORE-VALENCE EXCHANGE AND NO VALENCE SOC

Here, we prove analytically the numerical results of Fig. 4. We start with several definitions. The circular dichroism $\Delta F(\hat{\mathbf{k}}, \mathbf{L}) = F^+(\hat{\mathbf{k}}, \mathbf{L}) - F^-(\hat{\mathbf{k}}, \mathbf{L})$, which is the difference of the absorption spectra for the right-hand and left-hand circularly polarized light, can be obtained from the Fermi golden rule

$$F^\pm(\hat{\mathbf{k}}, \mathbf{L}) = \sum_f |\langle f_{\mathbf{L}} | \hat{T}_{\hat{\mathbf{k}}}^\pm | i_{\mathbf{L}} \rangle|^2 \delta(\omega - E_{fi;\mathbf{L}}). \quad (\text{A1})$$

Here, $|i_{\mathbf{L}}\rangle$ and $|f_{\mathbf{L}}\rangle$ are the eigenstates of the Hamiltonian, $E_{fi;\mathbf{L}}$ is the excitation energy, and $\hat{T}_{\hat{\mathbf{k}}}^\pm$ are the dipole operators for the right- and left-hand polarization with respect to propagation vector $\hat{\mathbf{k}}$. Owing to the immobility of the core hole the x-ray absorption spectrum is a sum over site contributions.

We will use the geometry of Fig. 6 with the x rays coming along the x axis and the quantization z axis of spin and angular momenta parallel to the crystallographic c axes. To evaluate XMCD $\Delta F^{(a)}$ and $\Delta F^{(b)}$ for the geometries for Figs. 4(a) and 4(b) we will vary the angles φ (orientation of the crystal) and α (orientation of the local moment)

$$\begin{aligned} \Delta F^{(a)} &= \frac{1}{2} \left[\Delta F(0, 0) + \Delta F\left(\frac{\pi}{2}, \pi\right) \right], \\ \Delta F^{(b)} &= \Delta F\left(\frac{\pi}{4}, \frac{\pi}{2}\right). \end{aligned} \quad (\text{A2})$$

Here, we use the angles φ and α in $\Delta F(\varphi, \alpha)$ to represent $\hat{\mathbf{k}}$ and \mathbf{L} in the geometry of Fig. 6. Using the relations between

the dipole operators \hat{T}^x , \hat{T}^y , and \hat{T}^z ,

$$\begin{aligned} T^+ &= -T^x - iT^y, \\ T^- &= -T^x + iT^y, \quad T^0 = T^z, \end{aligned}$$

we express the dipole operators $T_{\hat{x}}^{\pm}$ for the circularly polarized light propagating along the x -axis, helicity basis for $\hat{\mathbf{k}} \parallel x$, using dipole operators in the helicity basis for $\hat{\mathbf{k}} \parallel z$ [52]. We drop the \hat{z} subscript in $T_{\hat{z}}^{\pm}$ for sake of readability.

$$T_{\hat{x}}^{\pm} = -T^y \mp iT^z = i \left(\frac{T^+ - T^-}{2} \pm T^0 \right).$$

The expression (A1) for XMCD then takes the form

$$\begin{aligned} \Delta F(\varphi, \alpha) &= \sum_f \langle f_{\varphi, \alpha} | \hat{T}^+ - \hat{T}^- | i_{\varphi, \alpha} \rangle \langle i_{\varphi, \alpha} | \hat{T}^0 | f_{\varphi, \alpha} \rangle \\ &\quad \times \delta(\omega - E_{fi}) + \text{c.c.} \\ &\equiv (T^+ - T^-) \overline{T^0} + \text{c.c.} \end{aligned} \quad (\text{A3})$$

Here, the polarization of the dipole operators is taken with respect to the z axis. We will use the shorthand notation for the matrix elements of the dipole operators shown on the third line from now on. In the absence of the valence SOC and core-valence multipole interaction, the excitation energy does not depend on the orientation of \mathbf{L} , i.e., on the angle α . The eigenstates for arbitrary angles φ and α can be obtained from those for $\varphi = 0$ and $\alpha = 0$ by a joint z -axis rotation $\mathcal{C}(\varphi, \alpha)$ of the core spin, core orbitals, and valence orbitals by angle φ , and rotation of the valence spin by angle α , which transform the operators

$$\mathcal{C}(\varphi, \alpha) : d_{m\sigma} \rightarrow e^{im\varphi} e^{i\sigma\alpha} d_{m\sigma}, \quad p_{m\sigma} \rightarrow e^{i(m+\sigma)\varphi} p_{m\sigma},$$

where m is the orbital and $\sigma = \pm \frac{1}{2}$ the spin projection along the z axis. Next, we use

$$\langle \mathcal{C}(\varphi, \alpha) f | \hat{T} | \mathcal{C}(\varphi, \alpha) i \rangle = \langle f | \mathcal{C}^{-1}(\varphi, \alpha) \hat{T} \mathcal{C}(\varphi, \alpha) | i \rangle$$

to transform the dipole operators instead of wave functions in (A3). Using the definition of the dipole operators

$$\begin{aligned} \hat{T}^{\pm} &\equiv \hat{T}_{\uparrow}^{\pm} + \hat{T}_{\downarrow}^{\pm} = \sum_{m, \sigma} \Gamma_{\pm m} \hat{d}_{m\pm 1\sigma}^{\dagger} \hat{p}_{m\sigma}, \\ \hat{T}^0 &\equiv \hat{T}_{\uparrow}^0 + \hat{T}_{\downarrow}^0 = \sum_{m, \sigma} \Gamma_m^{(0)} \hat{d}_{m\sigma}^{\dagger} \hat{p}_{m\sigma}, \end{aligned}$$

we arrive at their transformation properties

$$\begin{aligned} \mathcal{C}^{-1}(\varphi, \alpha) \hat{T}_{\sigma}^+ \mathcal{C}(\varphi, \alpha) &= e^{i\varphi} e^{-i\sigma(\varphi-\alpha)} \hat{T}_{\sigma}^+, \\ \mathcal{C}^{-1}(\varphi, \alpha) \hat{T}_{\sigma}^- \mathcal{C}(\varphi, \alpha) &= e^{-i\varphi} e^{-i\sigma(\varphi-\alpha)} \hat{T}_{\sigma}^-, \\ \mathcal{C}^{-1}(\varphi, \alpha) \hat{T}_{\sigma}^0 \mathcal{C}(\varphi, \alpha) &= e^{-i\sigma(\varphi-\alpha)} \hat{T}_{\sigma}^0. \end{aligned} \quad (\text{A4})$$

Substituting these into (A3) we get the formula for the XMCD spectra for general angles φ and α ,

$$\begin{aligned} \Delta F(\varphi, \alpha) &= (e^{i\varphi} T_{\uparrow}^+ - e^{-i\varphi} T_{\uparrow}^-) \overline{T_{\uparrow}^0} \\ &\quad + (e^{i\varphi} T_{\downarrow}^+ - e^{-i\varphi} T_{\downarrow}^-) \overline{T_{\downarrow}^0} \\ &\quad + (e^{i\alpha} T_{\uparrow}^+ - e^{-i(2\varphi-\alpha)} T_{\uparrow}^-) \overline{T_{\uparrow}^0} \\ &\quad + (e^{i(2\varphi-\alpha)} T_{\downarrow}^+ - e^{-i\alpha} T_{\downarrow}^-) \overline{T_{\downarrow}^0} + \text{c.c.} \\ &= (e^{i\alpha} T_{\uparrow}^+ - e^{-i(2\varphi-\alpha)} T_{\uparrow}^-) \overline{T_{\uparrow}^0} \\ &\quad + (e^{i(2\varphi-\alpha)} T_{\downarrow}^+ - e^{-i\alpha} T_{\downarrow}^-) \overline{T_{\downarrow}^0} + \text{c.c.} \end{aligned} \quad (\text{A5})$$

The $\uparrow\uparrow$ and $\downarrow\downarrow$ terms do not change sign under the magnetic moment reversal $\alpha \rightarrow \alpha + \pi$ and thus must vanish the expression for XMCD.

Now we can evaluate the XMCD spectra for the orientations in (A2):

$$\begin{aligned} \Delta F(0, 0) &= (T_{\uparrow}^+ - T_{\uparrow}^-) \overline{T_{\downarrow}^0} + (T_{\downarrow}^+ - T_{\downarrow}^-) \overline{T_{\uparrow}^0} + \text{c.c.}, \\ \Delta F\left(\frac{\pi}{2}, \pi\right) &= (-T_{\uparrow}^+ - T_{\uparrow}^-) \overline{T_{\downarrow}^0} + (T_{\downarrow}^+ + T_{\downarrow}^-) \overline{T_{\uparrow}^0} + \text{c.c.}, \\ \Delta F\left(\frac{\pi}{4}, \frac{\pi}{2}\right) &= (iT_{\uparrow}^+ - T_{\uparrow}^-) \overline{T_{\downarrow}^0} + (T_{\downarrow}^+ + iT_{\downarrow}^-) \overline{T_{\uparrow}^0} + \text{c.c.} \end{aligned} \quad (\text{A6})$$

Note that this is not enough to guarantee $\Delta F^{(a)} = \Delta F^{(b)}$. We use the fact that in the rutile structure there are twofold rotation axes parallel to $[110]$ and $[1\bar{1}0]$, i.e., $\varphi = 0$ and $\varphi = \frac{\pi}{2}$. In Ref. [28] we have shown that such rotation symmetry implies a vanishing of XMCD for the magnetic moment perpendicular to the x-ray propagation vector, i.e.,

$$\begin{aligned} \Delta F\left(0, \frac{\pi}{2}\right) &= (iT_{\uparrow}^+ - iT_{\uparrow}^-) \overline{T_{\downarrow}^0} + (-iT_{\downarrow}^+ + iT_{\downarrow}^-) \overline{T_{\uparrow}^0} \\ &\quad + \text{c.c.} = 0, \end{aligned}$$

$$\Delta F\left(\frac{\pi}{2}, \frac{\pi}{2}\right) = (iT_{\uparrow}^+ + iT_{\uparrow}^-) \overline{T_{\downarrow}^0} + (iT_{\downarrow}^+ + iT_{\downarrow}^-) \overline{T_{\uparrow}^0} + \text{c.c.} = 0.$$

Adding the two lines we get

$$iT_{\uparrow}^+ \overline{T_{\downarrow}^0} + iT_{\downarrow}^- \overline{T_{\uparrow}^0} + \text{c.c.} = 0, \quad (\text{A7})$$

and substituting (A7) into the third line of (A6) concludes the proof:

$$\begin{aligned} \frac{1}{2} \left[\Delta F(0, 0) + \Delta F\left(\frac{\pi}{2}, \pi\right) \right] &= -T_{\uparrow}^- \overline{T_{\downarrow}^0} + T_{\downarrow}^+ \overline{T_{\uparrow}^0} + \text{c.c.} \\ &= \Delta F\left(\frac{\pi}{4}, \frac{\pi}{2}\right). \end{aligned}$$

- [1] L. Šmejkal, A. H. MacDonald, J. Sinova, S. Nakatsuji, and T. Jungwirth, Anomalous Hall antiferromagnets, *Nat. Rev. Mater.* **7**, 482 (2022).
 [2] L. Šmejkal, R. González-Hernández, T. Jungwirth, and J. Sinova, Crystal time-reversal symmetry breaking and

spontaneous Hall effect in collinear antiferromagnets, *Sci. Adv.* **6**, eaaz8809 (2020).

- [3] K. Samanta, M. Ležaić, M. Merte, F. Freimuth, S. Blügel, and Y. Mokrousov, Crystal Hall and crystal magneto-optical effect in thin films of SrRuO₃, *J. Appl. Phys.* **127**, 213904 (2020).

- [4] M. Naka, S. Hayami, H. Kusunose, Y. Yanagi, Y. Motome, and H. Seo, Anomalous Hall effect in κ -type organic antiferromagnets, *Phys. Rev. B* **102**, 075112 (2020).
- [5] S. Hayami and H. Kusunose, Essential role of the anisotropic magnetic dipole in the anomalous Hall effect, *Phys. Rev. B* **103**, L180407 (2021).
- [6] I. I. Mazin, K. Koepf, M. D. Johannes, R. González-Hernández, and L. Šmejkal, Prediction of unconventional magnetism in doped FeSb₂, *Proc. Natl. Acad. Sci. USA* **118**, e2108924118 (2021).
- [7] R. D. Gonzalez Betancourt, J. Zubáč, R. Gonzalez-Hernandez, K. Geishendorf, Z. Šobáň, G. Springholz, K. Olejník, L. Šmejkal, J. Sinova, T. Jungwirth, S. T. B. Goennenwein, A. Thomas, H. Reichlová, J. Železný, and D. Kriegner, Spontaneous anomalous Hall effect arising from an unconventional compensated magnetic phase in a semiconductor, *Phys. Rev. Lett.* **130**, 036702 (2023).
- [8] M. Naka, Y. Motome, and H. Seo, Anomalous Hall effect in antiferromagnetic perovskites, *Phys. Rev. B* **106**, 195149 (2022).
- [9] L. Šmejkal, J. Sinova, and T. Jungwirth, Emerging research landscape of altermagnetism, *Phys. Rev. X* **12**, 040501 (2022).
- [10] M. Naka, S. Hayami, H. Kusunose, Y. Yanagi, Y. Motome, and H. Seo, Spin current generation in organic antiferromagnets, *Nat. Commun.* **10**, 4305 (2019).
- [11] R. González-Hernández, L. Šmejkal, K. Výborný, Y. Yahagi, J. Sinova, T. Jungwirth, and J. Železný, Efficient electrical spin splitter based on nonrelativistic collinear antiferromagnetism, *Phys. Rev. Lett.* **126**, 127701 (2021).
- [12] M. Naka, Y. Motome, and H. Seo, Perovskite as a spin current generator, *Phys. Rev. B* **103**, 125114 (2021).
- [13] H.-Y. Ma, M. Hu, N. Li, J. Liu, W. Yao, J.-F. Jia, and J. Liu, Multifunctional antiferromagnetic materials with giant piezomagnetism and noncollinear spin current, *Nat. Commun.* **12**, 2846 (2021).
- [14] L. Šmejkal, A. B. Hellenes, R. González-Hernández, J. Sinova, and T. Jungwirth, Giant and tunneling magnetoresistance in unconventional collinear antiferromagnets with nonrelativistic spin-momentum coupling, *Phys. Rev. X* **12**, 011028 (2022).
- [15] L. Šmejkal, J. Sinova, and T. Jungwirth, Beyond conventional ferromagnetism and antiferromagnetism: A phase with nonrelativistic spin and crystal rotation symmetry, *Phys. Rev. X* **12**, 031042 (2022).
- [16] S. W. Lovesey, D. D. Khalyavin, and G. van der Laan, Magnetic properties of RuO₂ and charge-magnetic interference in Bragg diffraction of circularly polarized x-rays, *Phys. Rev. B* **105**, 014403 (2022).
- [17] K.-H. Ahn, A. Hariki, K.-W. Lee, and J. Kuneš, Antiferromagnetism in RuO₂ as d -wave Pomeranchuk instability, *Phys. Rev. B* **99**, 184432 (2019).
- [18] S. Hayami, Y. Yanagi, and H. Kusunose, Momentum-dependent spin splitting by collinear antiferromagnetic ordering, *J. Phys. Soc. Jpn.* **88**, 123702 (2019).
- [19] L.-D. Yuan, Z. Wang, J.-W. Luo, E. I. Rashba, and A. Zunger, Giant momentum-dependent spin splitting in centrosymmetric low- Z antiferromagnets, *Phys. Rev. B* **102**, 014422 (2020).
- [20] L.-D. Yuan, Z. Wang, J.-W. Luo, and A. Zunger, Prediction of low- Z collinear and noncollinear antiferromagnetic compounds having momentum-dependent spin splitting even without spin-orbit coupling, *Phys. Rev. Mater.* **5**, 014409 (2021).
- [21] S. Hayami, Y. Yanagi, and H. Kusunose, Bottom-up design of spin-split and reshaped electronic band structures in antiferromagnets without spin-orbit coupling: Procedure on the basis of augmented multipoles, *Phys. Rev. B* **102**, 144441 (2020).
- [22] P. Liu, J. Li, J. Han, X. Wan, and Q. Liu, Spin-group symmetry in magnetic materials with negligible spin-orbit coupling, *Phys. Rev. X* **12**, 021016 (2022).
- [23] J. Yang, Z.-X. Liu, and C. Fang, Symmetry invariants and classes of quasi-particles in magnetically ordered systems having weak spin-orbit coupling, [arXiv:2105.12738](https://arxiv.org/abs/2105.12738).
- [24] Z. Feng, X. Zhou, L. Šmejkal, L. Wu, Z. Zhu, H. Guo, R. González-Hernández, X. Wang, H. Yan, P. Qin, X. Zhang, H. Wu, H. Chen, Z. Meng, L. Liu, Z. Xia, J. Sinova, T. Jungwirth, and Z. Liu, An anomalous Hall effect in altermagnetic ruthenium dioxide, *Nat. Electron.* **5**, 735 (2022).
- [25] B. T. Thole, P. Carra, F. Sette, and G. van der Laan, X-ray circular dichroism as a probe of orbital magnetization, *Phys. Rev. Lett.* **68**, 1943 (1992).
- [26] D. Weller, J. Stöhr, R. Nakajima, A. Carl, M. G. Samant, C. Chappert, R. Mégy, P. Beauvillain, P. Veillet, and G. A. Held, Microscopic origin of magnetic anisotropy in Au/Co/Au probed with x-ray magnetic circular dichroism, *Phys. Rev. Lett.* **75**, 3752 (1995).
- [27] J. Kuneš and P. M. Oppeneer, Anisotropic x-ray magnetic linear dichroism at the $L_{2,3}$ edges of cubic Fe, Co, and Ni: *Ab initio* calculations and model theory, *Phys. Rev. B* **67**, 024431 (2003).
- [28] A. Hariki, A. D. Din, O. J. Amin, T. Yamaguchi, A. Badura, D. Kriegner, K. W. Edmonds, R. P. Campion, P. Wadley, D. Backes, L. S. I. Veiga, S. S. Dhesi, G. Springholz, L. Šmejkal, K. Výborný, T. Jungwirth, and J. Kuneš, X-ray magnetic circular dichroism in altermagnetic α -MnTe, [arXiv:2305.03588](https://arxiv.org/abs/2305.03588).
- [29] N. Sasabe, M. Mizumaki, T. Uozumi, and Y. Yamasaki, Ferroic order for anisotropic magnetic dipole term in collinear antiferromagnets of $(t_{2g})^4$ system, *Phys. Rev. Lett.* **131**, 216501 (2023).
- [30] G. Khaliullin, Excitonic magnetism in Van Vleck type d^4 Mott insulators, *Phys. Rev. Lett.* **111**, 197201 (2013).
- [31] W. Metzner and D. Vollhardt, Correlated lattice fermions in $d = \infty$ dimensions, *Phys. Rev. Lett.* **62**, 324 (1989).
- [32] A. Georges, G. Kotliar, W. Krauth, and M. J. Rozenberg, Dynamical mean-field theory of strongly correlated fermion systems and the limit of infinite dimensions, *Rev. Mod. Phys.* **68**, 13 (1996).
- [33] G. Kotliar, S. Y. Savrasov, K. Haule, V. S. Oudovenko, O. Parcollet, and C. A. Marianetti, Electronic structure calculations with dynamical mean-field theory, *Rev. Mod. Phys.* **78**, 865 (2006).
- [34] T. Berlijn, P. C. Snijders, O. Delaire, H.-D. Zhou, T. A. Maier, H.-B. Cao, S.-X. Chi, M. Matsuda, Y. Wang, M. R. Koehler, P. R. C. Kent, and H. H. Weitering, Itinerant antiferromagnetism in RuO₂, *Phys. Rev. Lett.* **118**, 077201 (2017).
- [35] P. Blaha, K. Schwarz, G. Madsen, D. Kvasnicka, and J. Luitz, *WIEN2k, An Augmented Plane Wave + Local Orbitals Program for Calculating Crystal Properties* (Karlheinz Schwarz, Technische Universität Wien, Austria, 2001).
- [36] J. Kuneš, R. Arita, P. Wissgott, A. Toschi, H. Ikeda, and K. Held, Wien2wannier: From linearized augmented plane waves

- to maximally localized Wannier functions, *Comput. Phys. Commun.* **181**, 1888 (2010).
- [37] A. A. Mostofi, J. R. Yates, G. Pizzi, Y.-S. Lee, I. Souza, D. Vanderbilt, and N. Marzari, An updated version of wannier90: A tool for obtaining maximally-localised Wannier functions, *Comput. Phys. Commun.* **185**, 2309 (2014).
- [38] See Supplemental Material at <http://link.aps.org/supplemental/10.1103/PhysRevB.109.094413> for computational details and atomic model results.
- [39] M. Matsubara, T. Uozumi, A. Kotani, Y. Harada, and S. Shin, Polarization dependence of resonant x-ray emission spectra in early transition metal compounds, *J. Phys. Soc. Jpn.* **69**, 1558 (2000).
- [40] X. Wang, E. Gull, L. de' Medici, M. Capone, and A. J. Millis, Antiferromagnetism and the gap of a Mott insulator: Results from analytic continuation of the self-energy, *Phys. Rev. B* **80**, 045101 (2009).
- [41] L. Boehnke, H. Hafermann, M. Ferrero, F. Lechermann, and O. Parcollet, Orthogonal polynomial representation of imaginary-time Green's functions, *Phys. Rev. B* **84**, 075145 (2011).
- [42] H. Hafermann, K. R. Patton, and P. Werner, Improved estimators for the self-energy and vertex function in hybridization-expansion continuous-time quantum Monte Carlo simulations, *Phys. Rev. B* **85**, 205106 (2012).
- [43] P. Werner, A. Comanac, L. de' Medici, M. Troyer, and A. J. Millis, Continuous-time solver for quantum impurity models, *Phys. Rev. Lett.* **97**, 076405 (2006).
- [44] M. Jarrell and J. Gubernatis, Bayesian inference and the analytic continuation of imaginary-time quantum Monte Carlo data, *Phys. Rep.* **269**, 133 (1996).
- [45] A. Hariki, T. Uozumi, and J. Kuneš, LDA+DMFT approach to core-level spectroscopy: Application to 3d transition metal compounds, *Phys. Rev. B* **96**, 045111 (2017).
- [46] A. Hariki, M. Winder, and J. Kuneš, Continuum charge excitations in high-valence transition-metal oxides revealed by resonant inelastic x-ray scattering, *Phys. Rev. Lett.* **121**, 126403 (2018).
- [47] A. Hariki, M. Winder, T. Uozumi, and J. Kuneš, LDA + DMFT approach to resonant inelastic x-ray scattering in correlated materials, *Phys. Rev. B* **101**, 115130 (2020).
- [48] M. Winder, A. Hariki, and J. Kuneš, X-ray spectroscopy of the rare-earth nickelate LuNiO₃: LDA + DMFT study, *Phys. Rev. B* **102**, 085155 (2020).
- [49] The similarity of the L and M edge is not surprising since they both correspond to $p - d$ excitations, which are different only by core-valence interaction strength.
- [50] Z. Hu, H. von Lips, M. S. Golden, J. Fink, G. Kaindl, F. M. F. de Groot, S. Ebbinghaus, and A. Reller, Multiplet effects in the Ru $L_{2,3}$ x-ray-absorption spectra of Ru(IV) and Ru(V) compounds, *Phys. Rev. B* **61**, 5262 (2000).
- [51] J. Okamoto, T. Okane, Y. Saitoh, K. Terai, S.-I. Fujimori, Y. Muramatsu, K. Yoshii, K. Mamiya, T. Koide, A. Fujimori, Z. Fang, Y. Takeda, and M. Takano, Soft x-ray magnetic circular dichroism study of Ca_{1-x}Sr_xRuO₃ across the ferromagnetic quantum phase transition, *Phys. Rev. B* **76**, 184441 (2007).
- [52] We drop the \hat{z} subscript in $T_{\hat{z}}^{\pm}$ for the sake of readability.